Materials Science & Engineering C 126 (2021) 112192

Contents lists available at ScienceDirect

Materials Science & Engineering C

journal homepage: www.elsevier.com/locate/msec

Additively manufactured $BaTiO_3$ composite scaffolds: A novel strategy for load bearing bone tissue engineering applications

Elena Mancuso [a,*], Lekha Shah [b], Swati Jindal [a], Cecile Serenelli [a], Zois Michail Tsikriteas [c], Hamideh Khanbareh [c], Annalisa Tirella [b,*]

[a] Nanotechnology and Integrated Bio-Engineering Centre (NIBEC), Ulster University, Shore Road, BT37 0QB Newtownabbey, United Kingdom
[b] Division of Pharmacy and Optometry, School of Health Sciences, Faculty of Biology, Medicine and Health (FMBH), University of Manchester, Oxford Road, M13 9PT Manchester, United Kingdom
[c] Department of Mechanical Engineering, University of Bath, BA2 7AY Bath, United Kingdom

ARTICLE INFO

Keywords:
Barium titanate
PCL
Composite scaffolds
Bone tissue engineering
Additive manufacturing
Extrusion-based technology

ABSTRACT

Piezoelectric ceramics, such as $BaTiO_3$, have gained considerable attention in bone tissue engineering applications thanks to their biocompatibility, ability to sustain a charged surface as well as improve bone cells' adhesion and proliferation. However, the poor processability and brittleness of these materials hinder the fabrication of three-dimensional scaffolds for load bearing tissue engineering applications. For the first time, this study focused on the fabrication and characterisation of $BaTiO_3$ composite scaffolds by using a multi-material 3D printing technology. Polycaprolactone (PCL) was selected and used as dispersion phase for its low melting point, easy processability and wide adoption in bone tissue engineering. The proposed single-step extrusion-based strategy enabled a faster and solvent-free process, where raw materials in powder forms were mechanically mixed and subsequently fed into the 3D printing system for further processing.

PCL, PCL/hydroxyapatite and PCL/$BaTiO_3$ composite scaffolds were successfully produced with high level of consistency and an inner architecture made of seamlessly integrated layers. The inclusion of $BaTiO_3$ ceramic particles (10% wt.) significantly improved the mechanical performance of the scaffolds (54 ± 0.5 MPa) compared to PCL/hydroxyapatite scaffolds (40.4 ± 0.1 MPa); moreover, the presence of $BaTiO_3$ increased the dielectric permittivity over the entire frequency spectrum and tested temperatures. Human osteoblasts Saos-2 were seeded on scaffolds and cellular adhesion, proliferation, differentiation and deposition of bone-like extracellular matrix were evaluated. All tested scaffolds (PCL, PCL/hydroxyapatite and PCL/$BaTiO_3$) supported cell growth and viability, preserving the characteristic cellular osteoblastic phenotype morphology, with PCL/$BaTiO_3$ composite scaffolds exhibiting higher mineralisation (ALP activity) and deposited bone-like extracellular matrix (osteocalcin and collagen I).

The single-step multi-material additive manufacturing technology used for the fabrication of electroactive PCL/$BaTiO_3$ composite scaffolds holds great promise for sustainability (reduced material waste and manufacturing costs) and it importantly suggests PCL/$BaTiO_3$ scaffolds as promising candidates for load bearing bone tissue engineering applications to solve unmet clinical needs.

1. Introduction

Unlike in other tissues, most of bone injuries are able to heal spontaneously, thanks to the self-regeneration ability of human bone and without the need for further treatment [1,2]. However, in complex conditions such as critical size bone defects, or in cases where the regenerative process is compromised (i.e. atrophic non-unions, avascular necrosis and osteoporosis), additional reconstructive intervention is necessary. To overcome the shortcomings of traditional strategies (i.e. autografts, allografts and xenografts), tissue engineering emerged as a promising approach for the management of bone defects [3–6]. Over the past decades, the development of tissue-like substitutes, able to support bone healing in critical conditions, has been the main research focus within the field [2].

Inspired by the composition of native bone, which is primarily made up of collagen fibrils and hydroxyapatite (HA) crystals, the use of

* Corresponding authors.
E-mail addresses: e.mancuso@ulster.ac.uk (E. Mancuso), annalisa.tirella@manchester.ac.uk (A. Tirella).

https://doi.org/10.1016/j.msec.2021.112192
Received 2 April 2021; Received in revised form 9 May 2021; Accepted 14 May 2021
Available online 19 May 2021

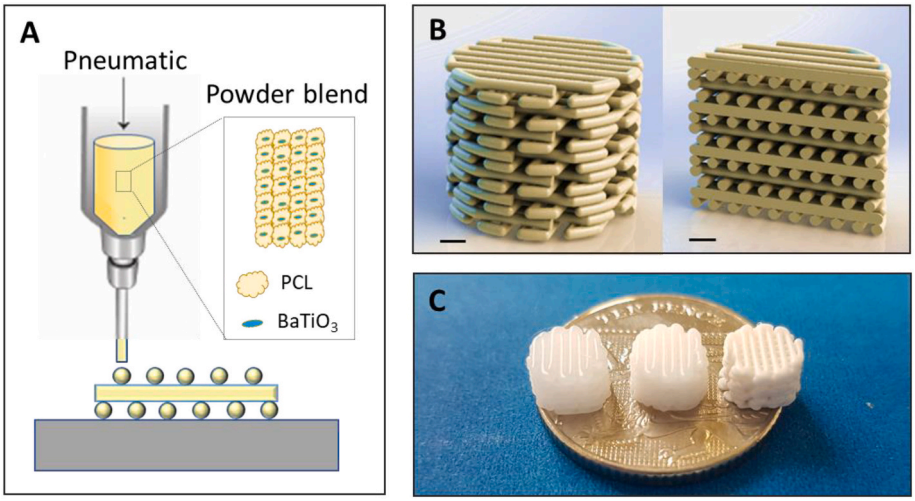

Fig. 1. Manufacturing of polymeric and composite scaffolds: A) Schematic representation of the extrusion-based additive manufacturing process; B) CAD model of the scaffold 3D volume and corresponding cross section (scale bar = 1 mm);C) representative image of the final 3D printed PCL (left), PCL/HA (centre) and PCL/$BaTiO_3$ (right) scaffolds.

composite materials has received great attention towards the development of bone tissue engineering scaffolds. Typical composite biomaterials fit to this purpose are polymeric matrix (e.g. polycaprolactone (PCL), polylactic acid (PLA)) filled with bioactive ceramic particles, including tricalcium phosphate (TCP), HA and its doped forms [7–10]. With this strategy, the already excellent characteristics of polymers to reproduce bone tissue features, such as biodegradability, processability and mechanical properties, are further improved with the inclusion of the bioactive ceramic phase to better mimic natural bone composition [7–10].

Moreover, electrical effects have been recently shown to play an important role in bone growth, remodelling and fracture healing [11]. Natural bone exhibits an electrical potential in response to mechanical stimuli due to its inherent piezoelectric property [12], manufacturing strategies to obtain composite scaffolds including bioactive materials capable of mimicking such property would pose a step stone to restore critical size bone defects. Among piezoelectric ceramics (i.e. lithium niobate, potassium sodium niobate and lithium-doped potassium sodium niobate), barium titanate ($BaTiO_3$) represents the most investigated lead-free piezoceramic [13]. In addition to its good biocompatibility and intrinsic capacity to sustain a charged surface, $BaTiO_3$ has shown great ability to improve bone cells' adhesion and proliferation [12,14].

In a study by Li et al., the incorporation of $BaTiO_3$ nanoparticles into randomly oriented poly-(l-lactic acid) (PLLA) electrospun scaffolds enhanced the osteogenic differentiation of bone marrow mesenchymal stem cells (MSCs) [15]. Etherami et al. found that the piezoelectric effect of highly porous $BaTiO_3$ scaffolds, produced through the conventional foam replication method and then coated with gelatine/HA, greatly improved the proliferation, differentiation, and extracellular matrix deposition of osteoblast-like cells [16]. Also, $BaTiO_3$ particles filled into a PCL/calcium sulfate whisker (15 wt%) matrix were used to prepare ternary composites. Even though the piezoelectric coefficient of the ternary composite decreased in comparison to the PCL/$BaTiO_3$, the presence of the calcium sulfate whisker contributed to enhance by 50% the flexural strength of the resulting composite and in the range of human cancellous bone [17].

Despite the combination of polymers and ceramics has contributed to address many of the limitations deriving from the use of single-phase biomaterials, scaffolds produced by conventional technologies still suffer from several shortcomings. Mainly they lack adequate control in terms of porosity and pore sizes, as well as mechanical properties and material composition throughout the structure. Also, they are inherently incapable to mimic complex architectures and with highly level of reproducibility for patient-specific applications [18,19]. Additionally, conventional biomanufacturing (i.e. solution electrospinning, freeze-drying, solvent casting) for the processing of composite materials often involves the use of organic solvents, whose inherent harmful effects further challenge their subsequent biological performances [15,17].

The design, architecture, porosity and fabrication methods are all crucial features that, together with biomaterial physico-chemical properties, contribute to the successful performance of a scaffold for bone tissue engineering, particularly in load bearing applications [20,21]. Additive manufacturing (AM) techniques, including binder jetting and fused deposition modelling (FDM), enable the design and fabrication of patient-specific substitutes with precise structural configurations [22–24] with higher degree of porosity and pore interconnectivity than conventional technologies [18,19]. Moreover, in the last decade AM technologies have greatly contributed to the design of bone tissue scaffolds with integrated and tailorable functionalities (including biochemical, electrical and mechanical) [25]. Recent studies have explored the development of composite scaffolds containing specific micro/nano-fillers, and which allow scaffolds to become bioactive [26,27], perform a specific function in response to an external stimulus (i.e. heat, light, magnetic field or pH) as well as change their shape or colour [28–31].

Although great achievements have been attained, the challenges in the processing of ceramic-based materials are still greatly hampering the manufacturing of 3D composite scaffolds with functional properties. In a recent study by Polley et al., $BaTiO_3$/HA composite scaffolds have been produced via binder jetting 3D printing. Although a good degree of customisation was achieved, along with a highly interconnected porous structure (open porosity = 50%), and piezoelectric properties comparable to human bone, due to their inherent brittleness the composite scaffolds showed very limited ability to withstand mechanical loadings (compressive strength of 150 ± 120 kPa) [32].

Furthermore, the processing and formulation of the raw materials often increase the complexity of the product development cycle as well as the manufacturing costs. Scaffolds produced by binder jetting generally require a final sintering step, which is necessary to consolidate the mechanical integrity of the printed structure. Whereas, FDM technologies require the additional extrusion step to produce a composite filament, which is then used to produce 3D scaffolds [33]. Lately, several studies, including some of the authors, have demonstrated the advantages in using multi-material extrusion-based AM technology as

Table 1
Summary of processing conditions used to fabricate polymeric PCL scaffolds, PCL/HA and PCL/$BaTiO_3$ composite scaffolds.

Sample	Composition (wt%)	Printing temperature (°C)	Printing pressure (bar)	Printing speed (mm/s)	Pre/post flow (s)
PCL	100	130	6	0.6	0.75/0.10
PCL/HA	90/10	130	6.5	0.5	0.75/0.10
PCL/$BaTiO_3$	90/10	125	5.5	0.7	0.75/0.10

emergent manufacturing approach for the production of composites scaffolds [9,34–37]. Although, to the best of our knowledge, only limited research has been conducted so far to exploit this environmentally friendly and versatile strategy for the manufacture of biodegradable composites based on piezoelectric materials.

Given the existing evidence that piezoelectric characteristics of $BaTiO_3$ have positive effects on natural bone formation pathways [12,14], and to enable its wider adoption in load bearing tissue engineering applications, in this study we focused on the fabrication, characterisation and biological validation of composite PCL scaffolds incorporating $BaTiO_3$ particles. PCL was selected as polymeric matrix material due to its thermoelastic behaviour, low melting point and ease of processing, remarkable mechanical strength, biocompatibility, as well as being an FDA approved biodegradable polymer. The physicochemical, mechanical and electrical properties of the additively manufactured PCL/$BaTiO_3$ scaffolds were assessed and compared against pure PCL and PCL/HA. The addition of $BaTiO_3$ ceramic particles increased both the mechanical performance and the dielectric permittivity, with decreased dielectric loss in the composite scaffolds.

All tested scaffolds supported the adhesion of human osteoblasts (i.e. Saos-2), with increased proliferation and extracellular matrix deposition in both PCL/HA and PCL/$BaTiO_3$ scaffolds up to 28 days. In particular, after incubation with mineralisation media, calcium phosphate and osteocalcin deposition were observed in both composite scaffolds; the increased deposition of collagen I in PCL/$BaTiO_3$ scaffolds may suggests this configuration as more suitable in load bearing bone tissue engineering applications.

2. Materials and methods

2.1. Design and manufacturing of 3D scaffolds

PCL powder (Mw = 40,000–50,000, Mn = 45,000 and particle size <600 μm) was purchased from Polyscience Europe (Germany), $BaTiO_3$ powder (D90 = 4.0 μm) was purchased from Ferro Ltd. (UK), and sintered HA was supplied by the Biomaterials Innovation and Development Centre of Riga Technical University (Riga, Latvia) and produced as reported in [9].

Scaffold manufacturing (Fig. 1A) was performed as previously described [9,34]. For composite scaffolds, the powder-based materials were homogeneously mixed with 10% wt. ceramic content, as reported in Table 1. The powder was placed into heated metal cartridges and extruded following optimised parameters through a blunt tip needle (0.4 mm inner diameter) and by using a commercial 3D Bioplotter extrusion system (EnvisionTEC, Germany). 3D porous cylindrical models (3 and 6 mm height, 7 mm diameter) were designed in Solid Edge™ 3D software, then the Computer-aided design (CAD) model was uploaded into Perfactory Software Suite (EnvisionTEC, Germany) and sliced to obtain 420 μm slicing thickness (Fig. 1B). Cylindrical specimens were printed continuously, with a spacing of 0.8 mm between strands and an offset between each layer equal to half of the strands' distance (Fig. 1C).

2.2. Physicochemical characterisation and mechanical properties evaluation

2.2.1. Attenuated total reflectance Fourier transform infrared spectroscopy (ATR-FTIR)

The composition of raw materials was analysed via Attenuated Total Reflectance Fourier Transform Infrared Spectroscopy (ATR-FTIR) using a Nicolet iS5 (Thermo Scientific, UK) system, equipped with an iD5 ATR diamond crystal window. FTIR spectra were recorded in the range of 400–4000 cm^{-1}.

2.2.2. Thermogravimetric analysis (TGA)

In order to assess the ceramic content in the extruded filaments after printing as well as their thermal behaviour upon heating, thermogravimetric analysis (TGA) was performed. The analyses were performed in nitrogen atmosphere by using a TGA2 METTLER TOLEDO™ instrument with a resolution of 1 μg and weighing accuracy of 0.005%. All the samples (PCL, PCL/HA and PCL/$BaTiO_3$), with an initial weight of ~15 mg, were tested in the range of temperature between 50 and 600 °C at a heating rate of 10 °C/min.

2.2.3. Imaging: scanning electron microscopy (SEM) and micro–computed tomography (micro-CT)

The microstructure of the printed composite scaffolds and the dimension of the printed strands was measured using images acquired by Scanning Electron Microscopy (Hitachi FE-SEM SU5000) at voltage of 3.0 kV and working distance between 5 and 8 mm. In addition to this, the 3D architecture of the scaffolds and the distribution of the bioceramic phases were evaluated by using a micro–Computed Tomography (micro-CT) scanner (Skyscan 1275, Bruker, Belgium) equipped with a source voltage of 40 kV and a current of 250 μA, setting the pixel detector resolution to 10 μm. All the scaffolds were scanned with a 49 ms exposure in a 360 scan with 0.2° increment to improve image quality and reduce noise. For image reconstruction, the Bruker NRecon Software (Bruker, Belgium) was used with 15% beam hardening reduction and no ring artefact reduction. The overall porosity of the scaffolds was calculated theoretically from the CAD design as reported by Moroni et al. [38], and also experimentally through the actual dimensions of the specimens (n = 3) measured from the 2D sections, and by using the Brucker CTAn software.

2.2.4. Mechanical properties

The mechanical properties of the scaffolds were measured via uniaxial compressive tests. For this purpose, cylindrical samples were printed with diameter of 7 mm and thickness of 6 mm (a total of 12 layers). Tests were performed using a universal testing machine (Instron 5500S, Instron, UK) equipped with a 500 N load cell. The uniaxial testing was conducted at a constant loading rate of 0.5 mm/min and maximum loading of 490 N. All the specimens (n = 5) were subjected to a preload of 2 N before starting of the test. All tests were performed on dry samples at room temperature. The modulus was calculated from the linear range of the stress–strain curve for each sample. All experimental data are presented as mean ± standard deviation (SD).

2.3. Dielectric and piezoelectric properties

The electrical response of the printed composite scaffolds was examined through impedance spectroscopy using a 1260A Impedance/

Gain-Phase Analyzer (Solartron Analytical, UK). The fabricated composites were tested in the frequency range from 0.1 Hz to 100 kHz at room temperature (RT) and 40 °C. A poling study was performed using a Corona poling set-up and the effect of time, temperature, and the electric field strength on the poling efficiency of the composites was studied. Firstly, poling was performed at room temperature by varying the applied voltage (5 kV, 10 kV, 15 kV and 20 kV) for 5 h in each individual voltage. Afterwards, the composites were poled with an applied potential of 20 kV at increasing applied temperatures (40 °C, 45 °C, 50 °C and 55 °C), while held for 5 h at each individual one. The d_{33} values of the composites were recorded after each poling step using a d_{33} Berlincourt piezometer supplied by Piezotest at 97 Hz. The polarisation-electric field (P-E) hysteresis loops were recorded using the Sawyer-Tower circuit at 100 Hz and room temperature with a high-voltage amplifier (Precision RT66C Ferroelectric Tester) supplied by Radiant Technologies.

2.4. In vitro cell studies

2.4.1. Cell culture

Human bone osteosarcoma Saos-2 cell line was kindly provided by Dr. Olga Tsikou (The University of Manchester) and maintained in McCoy's 5A media (M9309, Sigma-Aldrich, UK) supplemented with 15% *v*/v FBS (10,500,064, Gibco, UK) and 1% v/v penicillin-streptomycin (P0781, Sigma-Aldrich, UK). Cells were cultured in standard cell culture conditions (37 °C, 5% CO_2), passaged when reached confluency and kept at a cell density of 3×10^5 cells/cm^2. Prior use, Saos-2 were tested Mycoplamsa negative by Mycoalert mycoplasma detection kit (Lonza, UK). All the experiments were performed with Saos-2 from passage 11 to passage 20, then cells were discarded.

2.4.2. Scaffold cell seeding and mineralisation protocol

Scaffolds were sterilised prior to cell seeding as previously described [9]. All the following steps were performed in a class II biological safety cabinet. Briefly, scaffolds were immersed in 70% *v*/v ethanol (aq.) and incubated for 20 min at RT; scaffolds were washed three times with 1× PBS. The scaffolds were placed in a non-TC treated sterile 48 well plate and further exposed to UV-C light for 30 min each side. After sterilisation, 2×10^5 Saos-2 cells were suspended in 50 μL volume of complete media and gently pipetted on the top of each scaffold. Scaffolds were incubated for 30 min (37 °C, 5% CO_2) allowing cell adhesion, then a volume of 400 μL of complete media was gently pipetted in each well covering the whole scaffold. Cell culture media was replaced after 4 days, and after 7 days of culture (37 °C, 5% CO_2), the culture media was changed to Osteoblast mineralisation media (C-27020, PromoCell) to induce mineralisation and changed thereafter every 4 days and until the end point (i.e. day 28).

2.4.3. Proliferation assay

Cell proliferation was quantified by Alamar blue assay using Deep blue cell viability reagent (424,702, BioLegend, UK). Briefly, at each time point, cell culture media was removed from each well and replaced with a 400 μL volume of 10% *v*/v deep blue viability reagent in complete media. Cells were incubated for 2 h (37 °C, 5% CO_2), then a volume of 200 μL was transferred to a 96 well plate and the fluorescence was measured using a plate reader (Ex 530–570 nm/Em 590–620 nm, Synergy-2, Biotek, UK). After each time point, a 400 μL volume of complete fresh media was added to each well, avoiding any interference in future readings. Of note and prior to each measurement, the scaffolds were transferred to a new sterile well plate to measure proliferation of cells on the scaffold only. Experiments were performed in triplicate for each time point and type of scaffold tested and repeated for biological duplicate. For each scaffold and time point, data are presented as mean ± SD ($n = 2$, $N = 3$).

2.4.4. Alkaline phosphatase activity (ALP) assay

At selected time points, cells were fixed with 4% *v*/v formaldehyde solution (1004968350, Sigma-Aldrich UK) for 10 min followed by washes with 1× PBS. The cells were then permeabilised with a solution of 0.1% v/v Triton-X in 1× PBS for 15 min and finally washed three times with 1× PBS . Cellular alkaline phosphatase activity (ALP) was quantified for each type of scaffold tested ($n = 3$) using ALP Diethanolamine activity kit (AP0100, Sigma-Aldrich, UK) following manufacturer's instructions. Briefly, after permeabilization, a 1 mL volume of ALP reaction buffer was added to the scaffolds. A 0.67 M pNPP substrate solution was prepared in ultrapure water and a 1 μL volume of this solution was added to the scaffolds, previously immersed in ALP buffer. Scaffolds were incubated for 15 min at 37 °C. The enzymatic activity was immediately measured with absorbance readings at 405 nm (Synergy-2 plat reader, Biotek, UK). Readings were converted to units/mL using a calibration curve obtained by measuring known amounts of ALP enzyme (U/mL) using the same method previously described and in the range of 0.15 U/mL and 10 U/mL. Finally, ALP activity was normalised to cell number, with each U/mL values divided by the cell proliferation reading (Alamar blue) measured for the corresponding scaffolds. For each scaffold and time point, data are presented as mean ± SD ($n = 2$, $N = 3$).

2.4.5. Alizarin-red staining and deposited calcium quantification

To quantify calcium deposition, scaffolds were fixed with 4% *v*/v formaldehyde solution at selected time points (day 21, day 28, n = 2, N = 3). After fixation, scaffolds were washed with ultrapure water and then incubated with Alizarin-red staining solution (TMS-008-C, Sigma-Aldrich, UK) for 15 min at room temperature on a plate shaker. Excess stain was removed by additional washes ($n = 3$) with ultrapure water, then scaffolds were washed with acetone ($n = 1$) and left to dry at room temperature. To quantify the reacted and deposited alizarin stain on the scaffolds, a 2 mL volume of 0.2 M NaOH:MeOH (1:1) solution was added to dissolve the stain for each scaffold, then a volume of 200 μL was transferred to another well-plate and measured by absorbance reading at 405 nm (Synergy-2 plate reader, Biotek, UK). A calibration curve obtained from known concentration of Alizarin red stain (mM) in 0.2 M NaOH:MeOH was used to calculate the deposited calcium. For each scaffold and time point, data are presented as mean ± SD ($n = 2$, $N = 3$).

2.4.6. Immunofluorescence staining and image acquisition

The morphology of Saos-2 cells on scaffolds was analysed by immunofluorescence staining using DAPI (Thermofisher, UK) and Alexa Fluor™ 488 Phalloidin (A12379, Thermofisher, UK) for nucleus and F-actin, respectively. Briefly, each scaffold was fixed with 4% *v*/v paraformaldehyde for 10 min and permeabilised with 0.1% Triton-X for 10 min at RT. After washes the scaffolds were incubated with a mix of DAPI (1 μg/mL) and Phalloidin (1:80) in 1× PBS for 30 min at RT and in the dark. Samples were washed three times with 1× PBS and stored immersed in 1× PBS at 4 °C in the dark.

Collagen I and osteocalcin immunofluorescence staining were performed on the scaffolds to detect any deposition of extracellular matrix after 28 days of culture. For this staining, scaffolds were fixed with 4% *v*/v paraformaldehyde for 5 min at RT, washed three times with 1× PBS and then incubated with blocking buffer (1% *w/v* BSA in 1× PBS) for 1 h at RT to avoid non-specific antibody binding. Scaffolds were washed with 1× PBS, and then incubated with Osteocalcin monoclonal antibody (1:500 dilution in 1× PBS, MA1-82975, Thermofisher, UK) and Collagen-I polyclonal antibody (1:250 dilution in 1× PBS, PA5-95137, Thermofisher, UK) overnight (16 h) at 4 °C. After three washes with blocking buffer, samples were incubated with a solution of secondary antibodies Goat anti-rabbit 488 (1:2000 dilution in 1× PBS, A-11008, Thermofisher, UK) and Goat anti-mouse 594 (1:2000 dilution in 1× PBS, A-11005, Thermofisher, UK) for 30 min at RT following manufacturers instruction. Samples were washed three times with blocking buffer and stored immersed in 1× PBS at 4 °C in the dark.

Images of scaffolds were acquired using the fluorescent inverted microscope (Leica DMI6000, Leica Microsystems, UK) coupled with a 5.5 Neo sCMOS camera (Andor, UK). The μManager software (v.1.46,

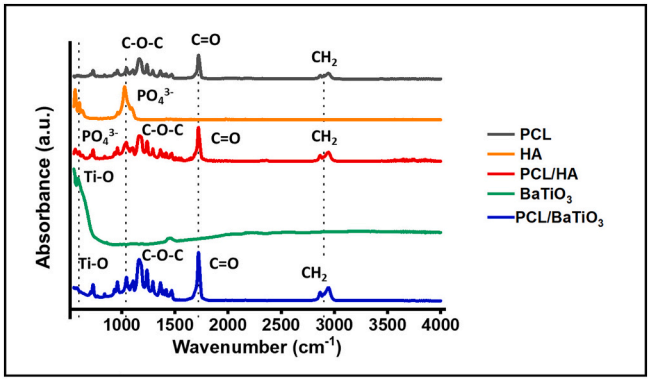

Fig. 2. FTIR spectra comparing PCL (black), HA powder (orange), $BaTiO_3$ powder (green), PCL/HA composite powder (red) and PCL/$BaTiO_3$ composite powder (blue). (For interpretation of the references to colour in this figure legend, the reader is referred to the web version of this article.)

Vale Lab, UCSF, USA) was used to control both microscope and camera, as well as to capture images. For acquisitions, a dry 10× objective (PL 10×/0.3 PH1, Leica), a dry 20× objective (PL 20×/0.5 PH2, Leica) and a dry 63× objective (PL 63×/0.9 PH2, Leica) with filter cubes (A4, I3 and N2.1) was used. All images were post-processed to remove background noise using ImageJ v1.49p.

2.5. Statistical analysis

For the mechanical analysis, differences between groups were determined by using a Paired *t*-test using a level of statistical significance $(p) < 0.05$. All experimental data are presented as mean ± SD.

For all cellular experiments, data are presented as average of at least three ($n = 3$) independent experiments ± SD, unless otherwise stated. One-way analysis of variance (ANOVA) with Brown-Forsythe and Welsh was performed using GraphPad Prism v9.1.0, as to analyse the significant differences among results for cell proliferation, ALP and Alizarin Red quantification. Probabilities were set at four different significance levels: $p < 0.05$ ($^{*}p \leq 0.05$, $^{**}p \leq 0.01$, $^{***}p \leq 0.001$, $^{****}p \leq 0.0001$).

Paired *t*-test was used to compare same scaffolds at different time points for Alizarin Red stain quantification. The *p*-values obtained are mentioned under the representative figure.

3. Results and discussion

3.1. Physicochemical and mechanical characterisation

ATR-FTIR analysis was performed on raw materials in order to confirm the presence of HA and $BaTiO_3$ inorganic phases into the mixed PCL-based powders. As reported in Fig. 2, both the PCL/HA and PCL/$BaTiO_3$ spectra showed the characteristic bands of PCL(Fig. 2, black line); specifically the C—H stretching (2943 and 2865 cm^{-1}), the C═O carbonyl group at 1720 cm^{-1}, the CH_2 deformation band 1165–1468 cm^{-1}, the backbone C—O and C—C stretching of the crystalline phase 1293 cm^{-1}, and the C—O—C symmetric and asymmetric band at 1239 cm^{-1}, 1164 cm^{-1}, 1107 cm^{-1}, 1047 cm^{-1} were detected [39]. Moreover, in the PCL/HA spectra (Fig. 2, red line) the characteristic peaks of pure HA were observed as: the O—H and $(PO_4)_3$ groups and respectively at 560, 600 and 1041 cm^{-1} [40]. The PCL/$BaTiO_3$ spectra (Fig. 2, blue line) showed the Ti—O stretching vibration peak at 559 cm^{-1} and the distinctive shape of $BaTiO_3$ spectrum (Fig. 2, green line), which confirmed the presence of this phase into the PCL/$BaTiO_3$ composite material [41]. Although the inorganic phases were incorporated at

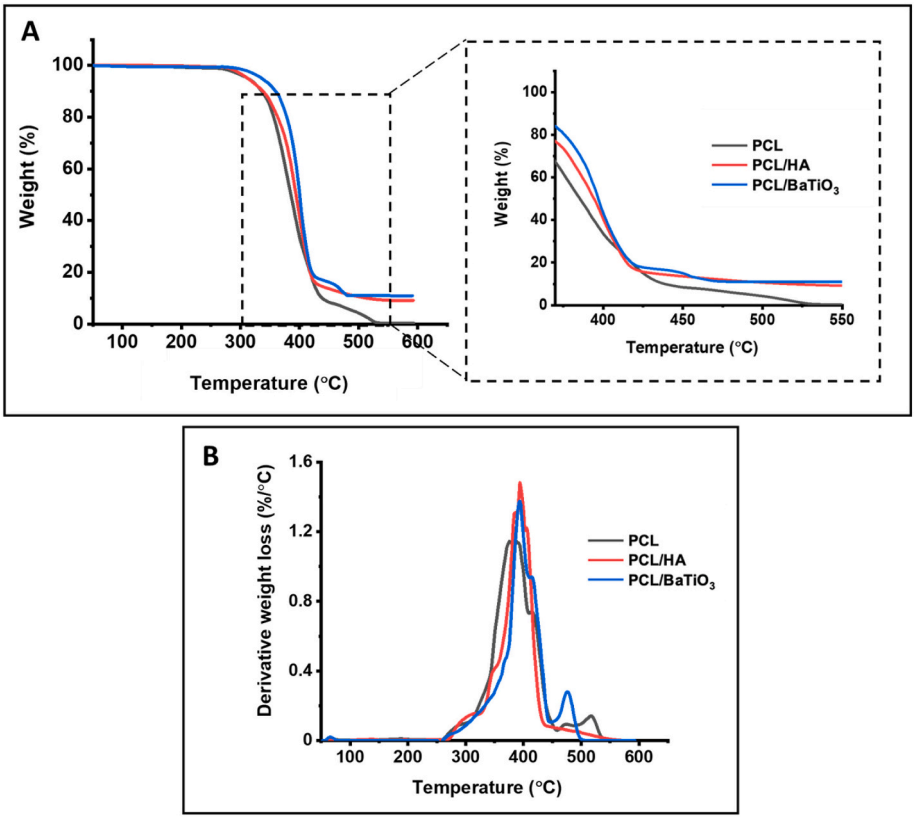

Fig. 3. Thermal characterisation of the samples after extrusion: (A) TGA thermograms and the zoom of the selected area indicating the remaining mass in each sample, and (B) TGA first derivative curves of PCL (black), PCL/HA (red) and PCL/$BaTiO_3$ (blue). (For interpretation of the references to colour in this figure legend, the reader is referred to the web version of this article.)

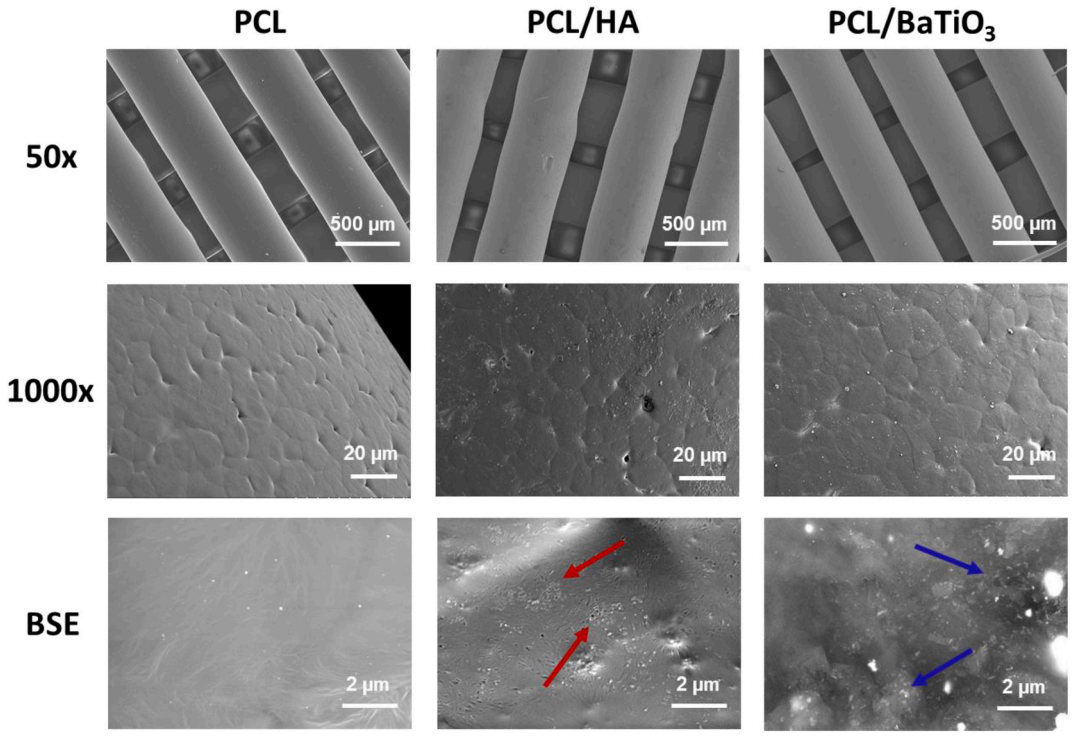

Fig. 4. SEM morphological evaluation of the 3D printed scaffolds at different magnifications showing strands and surface. Images acquired with the Backscattered Electron (BSE) mode evidenced the presence of HA (red arrows) and $BaTiO_3$ (blue arrows) particles. All images were captured using a top-view scan. (For interpretation of the references to colour in this figure legend, the reader is referred to the web version of this article.)

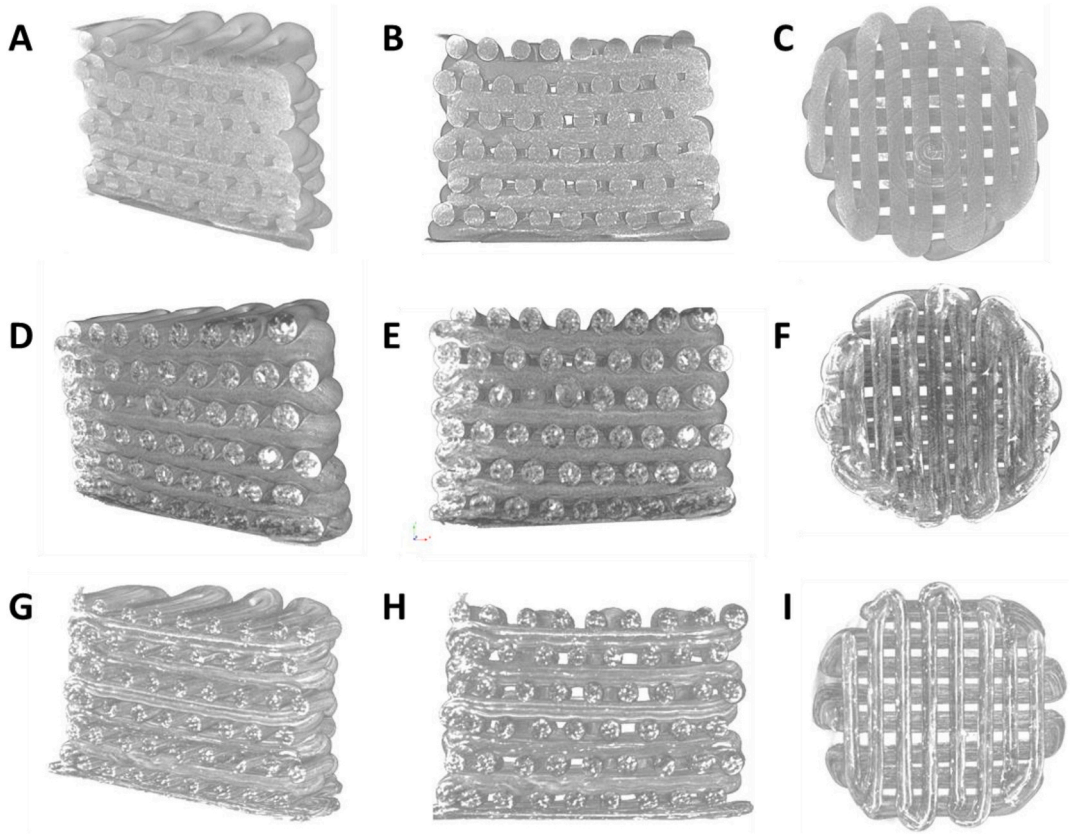

Fig. 5. Micro-CT reconstruction of PCL (A–C), PCL/HA (D—F) and PCL/$BaTiO_3$ (G–I) scaffolds. Cross sections (A–B, D–E, G–H) evidence the high-fidelity of printed scaffold towards the CAD model. All scaffolds show circular printed strand, homogeneous across the XY plane. Top view (C, F, I) showing the cylindrical shape of all scaffolds, as well as alignment of printed layers.

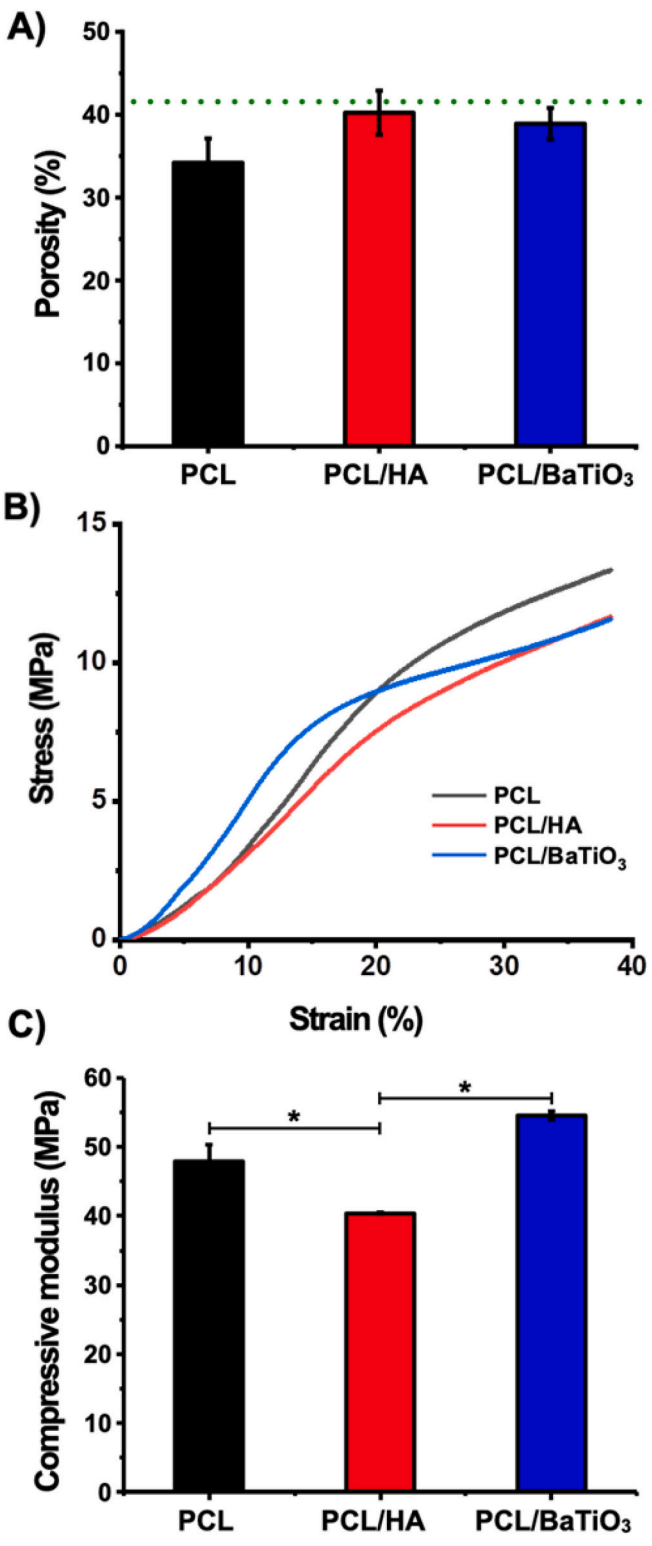

Fig. 6. A) Porosity values derived from micro-CT scans of the 3D scaffolds ($n = 3$) and theoretical porosity (green dotted line; results are presented as mean ± SD. B) Example of engineering stress-strain curves of PCL (black), PCL/HA (red) and PCL/$BaTiO_3$ (blue). All samples were compressed approximately until 40% strain. C) Compressive Modulus of each scaffold. The compressive modulus was calculated in the 0–10% strain interval; results represent mean ± SD ($n = 5$), $p < 0.05$ (*). (For interpretation of the references to colour in this figure legend, the reader is referred to the web version of this article.)

smaller amount (10% wt.) within the composite material, it was possible to detect their distinctive peaks via FTIR analysis.

TGA analysis was performed to evaluate the behaviour upon heating of the extruded materials and the amount of bioceramics incorporated within them (Fig. 3). Single step degradation and a pronounced mass loss was observed for all the samples (Fig. 3A). According to the analysis, a structural decomposition started at temperature above 250 °C, thus confirming the stability of all the compositions during the printing process. Both composite materials shown a slightly higher temperature requirement for degradation in comparison to pure PCL, with the 50% of the weight loss occurring at 385 °C, 395 °C and 405 °C for the PCL, PCL/HA and PCL/$BaTiO_3$ respectively. After 550 °C the remaining mass in the composite samples was relatively constant and content close to the theoretical value of 10% wt. (10.05 ± 1.3% wt. for PCL/HA and 12.5 ± 1.9% wt. for PCL/$BaTiO_3$ scaffolds). Also, as shown by the TGA first derivatives curves (Fig. 3B) the presence of the inorganic phases contributed to a slight shift in the maximum peaks towards higher temperatures, indicating the effect of the bioceramic particles in delaying the materials' degradation rate [42].

Scaffold morphology is known to greatly affect in vitro cell behaviour, with pore size, pores interconnectivity and surface characteristics, playing the most important role in promoting cell–scaffold interactions such as cell adhesion and migration, as well as proliferation [22,43]. SEM observations of the 3D printed scaffolds at low magnification (Fig. 4) showed the shifted pattern design and the resulting interconnected macro-porosity, matching the CAD design across all the scaffolds and proving the suitability of the printing process. A uniform strand diameter was measured across all groups, with an average strand diameter approximately 31 μm bigger than the theoretical target value (400 μm). This behaviour, observed across all the materials used in this study, is typical of viscoelastic polymer-based biomaterial inks, and due to its expansion upon extrusion from the nozzle [44]. At higher magnification (1000×) it was possible to appreciate the presence of uniformly distributed micro-pores on all the scaffolds. Moreover, no agglomeration or clumping of the ceramic particles was detected in any of the high-magnification images of the composite-based samples, supporting good mixing of the two materials prior printing.

Micro-CT analysis was performed to evaluate the overall scaffolds' architecture, as well as the inner structure of the 3D printed scaffolds. As shown in Fig. 5, the micro-CT reconstructions of all scaffolds evidenced a uniform geometry and a consistent structural integrity along with a high fidelity to the CAD model dimensions. Regular pore size and defined circular cross-sections of the printed filament was observed in the cross-sectional reconstructions across all the groups (Figs. 5B, 5E, 5H). From these datasets, it is also evidenced the uniform distribution of the ceramic phase in the PCL matrix for the composite-based scaffolds, further supporting the appropriate mixing step of the raw materials [45]. Experimental data derived from the micro-CT reconstructions also supported the assessment of the 3D scaffolds' porosity.

As shown in Fig. 6A all the printed samples displayed similar porosity values, which were found between 35% and 45%, as expected theoretically (41.6%) and within the range of porosity of human cancellous bone [46]. Notably, no statistical difference was observed across samples. Obtained results prove the suitability of the extrusion-based approach towards the manufacturing of composite scaffolds with highly interconnected structures and reproducible architectures.

Mechanical performances represent a key requirement for bone scaffolds, particularly in load bearing applications, as they need to match the host tissue mechanical characteristics and withstand physiological forces imposed on the structure [6,20,43]. In this study, the mechanical properties of the scaffolds were measured using cylindrical samples (diameter 7 mm, thickness 6 mm) tested under uniaxial compressive loading to investigate the role of the bioceramic phase included in the polymeric matrix. Fig. 6B shows representative stress-strain curves of PCL (black), PCL/HA (red) and PCL/$BaTiO_3$ (blue) scaffolds. All the tested scaffolds showed a stress-strain response

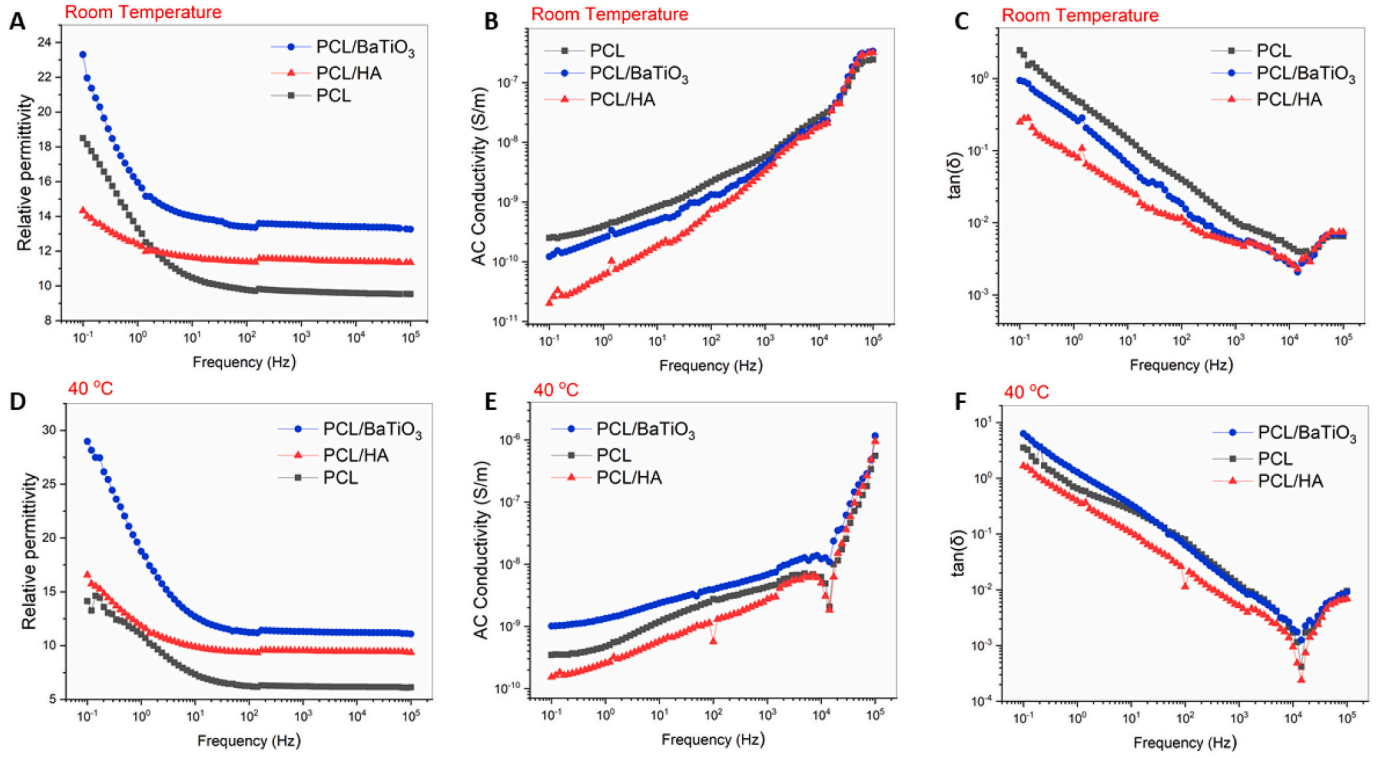

Fig. 7. Dielectric response of scaffolds: A) Real part of dielectric permittivity, B) AC conductivity (S/m) and C) Loss tangent (tanδ) as a function of frequency (Hz) for the PCL (black), PCL/HA (red) and PCL/$BaTiO_3$ (blue) composites at RT, D) Real part of dielectric permittivity, E) AC conductivity (S/m) and F) Loss tangent (tanδ) as a function of frequency (Hz) for the PCL (black), PCL/HA (red) and PCL/$BaTiO_3$ (blue) composites at 40 °C. (For interpretation of the references to colour in this figure legend, the reader is referred to the web version of this article.)

characterised by an initial linear elastic region up to 10% compression strain, followed by densification and the eventual rupture of the samples at approx. 40% strain. As shown in Fig. 6C the inclusion of $BaTiO_3$ particles into the polymeric matrix led to a composite structure with significantly improved mechanical performance when compared to pure PCL and PCL/HA composite scaffolds. This outcome might be attributed to the particles acting as strain absorbers within the polymeric matrix [47,48]. According to the published literature focusing on 3D printed scaffolds, in addition to the design features (including shape, size pore size and strand dimension), it is reported that physicochemical properties play a crucial role towards their mechanical performance [19,46,49]. While several studies have reported that the incorporation of inorganic fillers (up to 10% wt.) improves composite scaffold mechanical properties [50,51], there are as much demonstrating their adverse effect [9,36]. Considering the characteristics of the scaffolds produced in this study and with reference to the reproducibility in terms of strand dimensions, the high fidelity to the CAD model and the similar porosity values across all the groups, it is likely that the increased compressive modulus measured in the PCL/$BaTiO_3$ scaffolds is the result of the actual material composition, irrespective of the geometrical features. In particular, the higher density of $BaTiO_3$ (6 g/cm^3) in comparison to HA powder (~3 g/cm^3) could be responsible for the higher compressive modulus. Our results suggest that the inclusion of 10% wt. of $BaTiO_3$ particles enhanced the mechanical properties of the PCL/$BaTiO_3$ composite scaffolds, fabricated for the first time via a single-step additive manufacturing technology and in comparison to ceramic-based composites manufactured using binder jetting 3D printing [32].

3.2. Electroactive properties

Fig. 7A–C present the room temperature dielectric permittivity, AC conductivity and dielectric loss plots of the printed composite scaffolds as a function of frequency. Fig. 7D–F show the dielectric permittivity, AC conductivity and dielectric loss at 40 °C, respectively. The dielectric properties are investigated at RT and 40 °C as the poling study has been performed at these two temperatures. As observed in Fig. 7A and D, the inclusion of both HA and $BaTiO_3$ particles increase the relative permittivity with respect to pristine PCL scaffolds, with PCL/$BaTiO_3$ scaffolds showing the highest permittivity values over the entire frequency spectrum at both tested temperatures. This is in agreement with the reported dielectric behaviour of PCL/$BaTiO_3$ composites [52].

Relative permittivity values of all scaffolds at both RT and 40 °C increase with decrease of the applied frequency as the dipoles attain sufficient time to reorientate in the direction of the electric field [53]. A strong electrode polarisation is observed at low frequencies, which reduces with increasing frequencies as expected for dielectric polymers and particulate composites [54]. However, at RT, the increase of PCL/HA's permittivity values do not follow the same trend as PCL and PCL/$BaTiO_3$ samples, PCL/HA exhibits lower slope in the low frequency region ($f < 10$ Hz) than the other two types of samples leading in lower values of permittivity than pristine PCL. This is likely due to a strong adhesion between the HA particles and the polymer chain leading to immobilization of the macromolecular chain or even entanglement which in turn reduces the dielectric response of the polymer to the applied electric field, thus decreasing the permittivity [55,56]. The $BaTiO_3$ particles on the other hand do not show this adverse effect and effectively increase the dielectric permittivity of PCL even at the relatively low weight fractions used in this study.

The measured AC conductivity at RT (Fig. 7B) and 40 °C (Fig. 7E) shows the presence of flat, dispersive, and linear regions as a function of frequency, in agreement with the reported behaviour for PCL in literature [52]. The dielectric loss factor (tan (δ)) behaviour of the composites as a function of frequency measured at RT (Fig. 7C) and 40 °C (Fig. 7F) showed an increase in dielectric loss is in accordance with the increase in real permittivity at low frequencies. The phenomenon observed in the high-frequency region ($f > 10{,}000$ Hz) can be attributed to interfacial

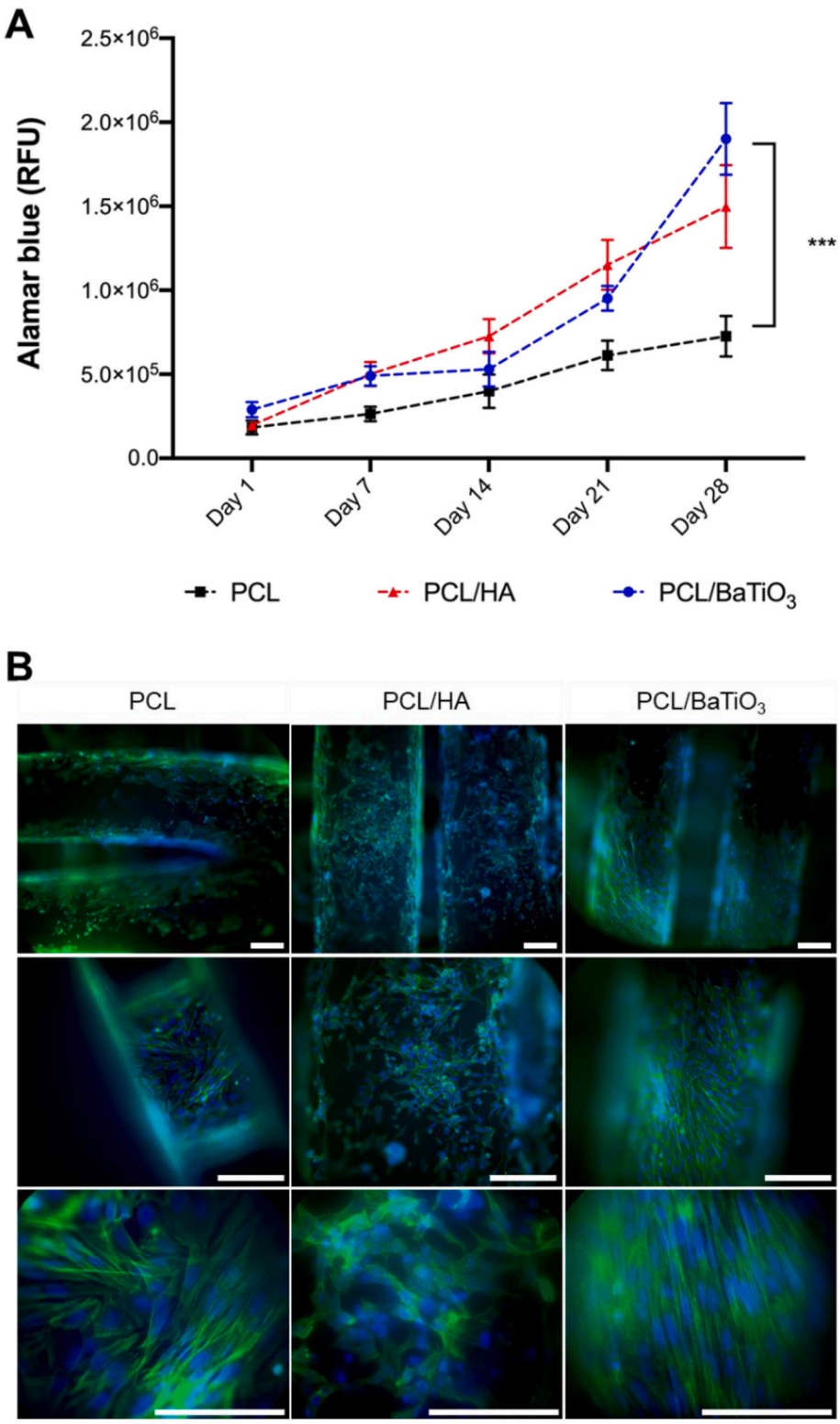

Fig. 8. A) Proliferation assay of Saos-2 cell lines when cultured in PCL (black), PCL/HA (red) and PCL/$BaTiO_3$ (blue) scaffolds. Cell proliferation was measured by Alamar blue fluorescence at different time points and up to day 28 showing higher proliferation in both PCL/HA and PCL/$BaTiO_3$ composite scaffolds compared to pristine PCL scaffolds at day 28. Statistical analysis at day 28 using One-way ANOVA returned: PCL vs PCL/$BaTiO_3$ p-value <0.001 (**),PCL vs PCL/HA p-value <0.05 (*), and no significance between PCL/HA vs PCL/$BaTiO_3$. Data are presented as mean ± SD ($n = 2$, $N = 3$). B) Morphology of Saos-2 cell lines in PCL, PCL/HA and PCL/BaTiO3 scaffolds. Immunostained images of Saos −2 cells at day 28 in tested 3D composite scaffolds. Nucleus stained is by DAPI (blue) and actin stained by Phalloidin alexa fluor 488 (green) and imaged at different magnification using inverted microscope. Scale bars 200 μm. (For interpretation of the references to colour in this figure legend, the reader is referred to the web version of this article.)

polarisation occurring at the interface of the crystalline and the amorphous phase of the PCL polymer due to ionic motions [53] and it seems to be more intense in the composite scaffolds compared to the pristine PCL. This is due to the fact that in the composite scaffolds, interfaces are formed between polymer matrix and ceramic inclusions as well as the crystalline and the amorphous phase of the polymer.

The poling study performed at RT and 40 °C, for up to 5 h at the varying electric field of 5, 10, 15 and 20 kV/mm resulted in d_{33} values lower than 0.1 pC/N, indicating the effect of low fraction of the ferroelectric phase.

3.3. *In vitro evaluation of the 3D printed scaffolds*

3.3.1. *Cytocompatibility*

Saos-2 cell lines were chosen as an osteoblast model to test cytocompatibility and osteogenic potential of polymeric and composite

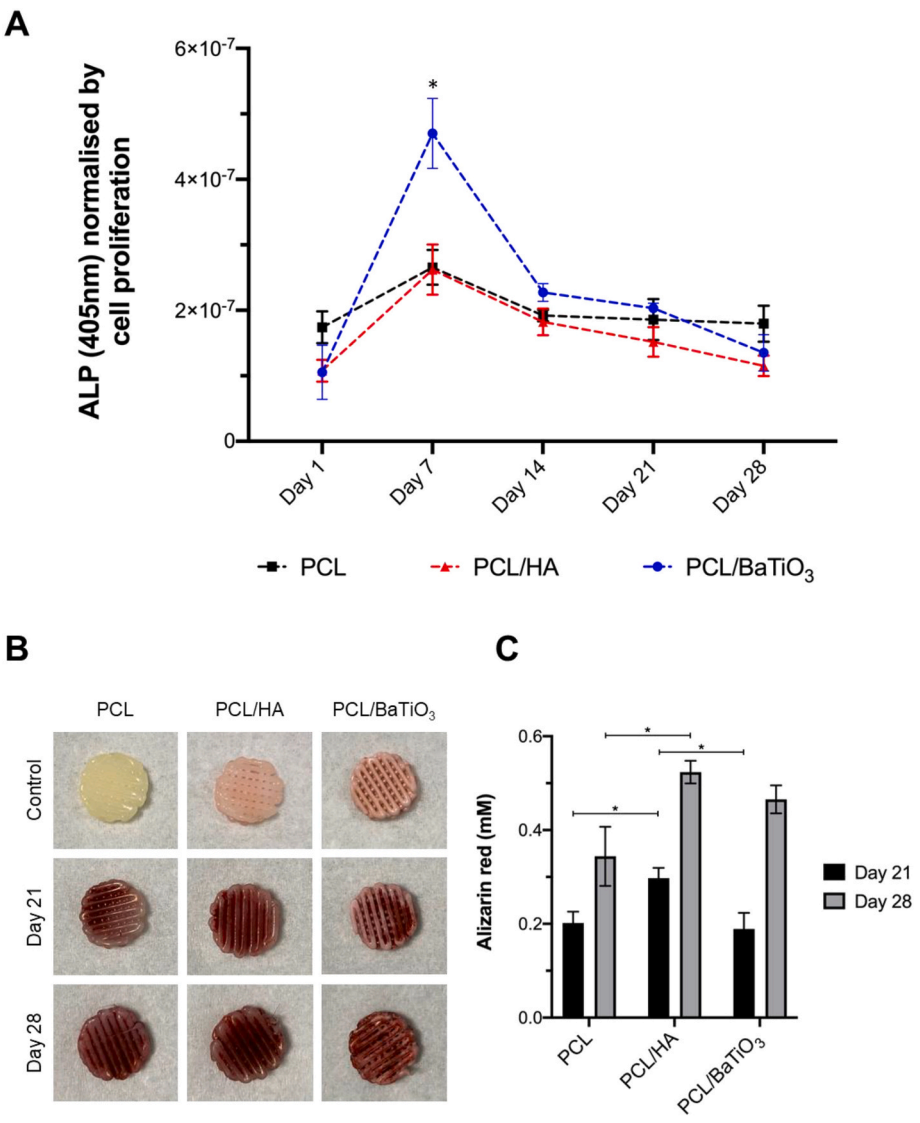

Fig. 9. Osteogenic activity of Saos-2 cells in PCL, PCL/HA and PCL/$BaTiO_3$ scaffolds. A) Alkaline phosphatase activity (ALP) of Saos-2 cells cultured in scaffolds at different time points and up to 28 days. The phosphatse activity was read at 405 nm. Statistics One-way ANOVA between PCL vs PCL/$BaTiO_3$ and PCL/HA vs PCL/$BaTiO_3$ p-value <0.05 (*), no significance was measured at all the other time points. B) Images of Alizarin stain on 3D scaffolds after 21 and 28 days of culture to highlighting calcium deposition by Saos-2 cells over time. C) Quantification of Alizarin stain by absorbance readings at 405 nm. Data are presented as mean ± SD ($n = 2$, $N = 3$). One-way ANOVA statistics is displayed in the figure, with significance levels $p < 0.05$ (*). Additional statistical analysis between each scaffold and at different time points (paired t-test) returned $p = 0.045$(*) for pristine PCL scaffolds, $p = 0.0107$(**) for PCL/HA scaffolds, and $p = 0.0019$ (**) for PCL/$BaTiO_3$ scaffolds.

scaffolds, as these cells were previously used in in vitro models for their osteogenic potential and mineralisation capability mimicking human osteoblasts [57,58].

Results show steady increase in cellular proliferation from day 1 to day 14 in all the scaffolds tested (Alamar blue viability assay, Fig. 8A), with increased proliferation rate in composite scaffolds from day 14 to day 28. Of note, cells have higher proliferation rate in PCL/$BaTiO_3$ scaffolds, such slower rate of proliferation from day 7 to day 14 could be attributed to the change in media from normal to mineralisation inducing media.

Fig. 8B shows uniform adhesion of Saos-2 cells after 28 days of culture on the scaffolds' strands, with no difference observed between pristine PCL and composite scaffolds (PCL/HA and PCL/$BaTiO_3$), as expected. Noticeably, Saos-2 cells were more uniformly adhered onto PCL/$BaTiO_3$ scaffolds when compared to PCL and PCL/HA scaffolds.

Moreover, images show similar Saos-2 cells alignment in PCL and PCL/$BaTiO_3$ scaffolds, with higher cell density and distinctive alignment in PCL/$BaTiO_3$ scaffolds visible at all the magnification. Morphology of Saos-2 cells cultured varied on different scaffolds and is better appreciated at higher magnifications (staining nuclei and F-actin, Fig. 8B). Saos-2 cells on pristine PCL and PCL/$BaTiO_3$ scaffolds are more elongated with spindle-like morphologies and higher attachments to the scaffolds' surface; whereas Saos-2 cells on PCL/HA scaffolds are less aligned and with a rather circular shape. Altogether, both proliferation and morphology show that PCL/$BaTiO_3$ showed higher cytocompatibility compared to pristine PCL and PCL/HA scaffolds, and confirms, suggesting a more functional osteoblast phenotype as also reported in literature [59,60].

3.3.2. *Osteogenic potential and mineralisation*

The osteogenic potential was tested by measuring cellular ALP activity, extracellular matrix deposition and mineralisation. Osteoblast culture maturation has been known to occur in three stages: first stage is characterised by growth, second stage by extracellular deposition of collagen and high ALP activity, and the third stage which marks complete maturation is characterised by matrix mineralisation (calcium phosphate and osteocalcin deposition) [61,62].

The addition of mineralisation media induces culture maturation to the third stage and hence the decrease in ALP activity is observed with consequent increase in calcium deposition (Fig. 9). Until the addition of mineralisation media at day 7, ALP activity as measured by the phosphatase activity on the pNPP substrate showed higher levels in PCL/$BaTiO_3$ scaffolds, demonstrating better osteogenic potential (Fig. 9A) when compared to PCL and PCL/HA scaffolds. Calcium deposition measured by alizarin stain and its quantification ((Fig. 9B) showed increasing trend from day 21 to day 28 in both composite scaffolds (i.e.

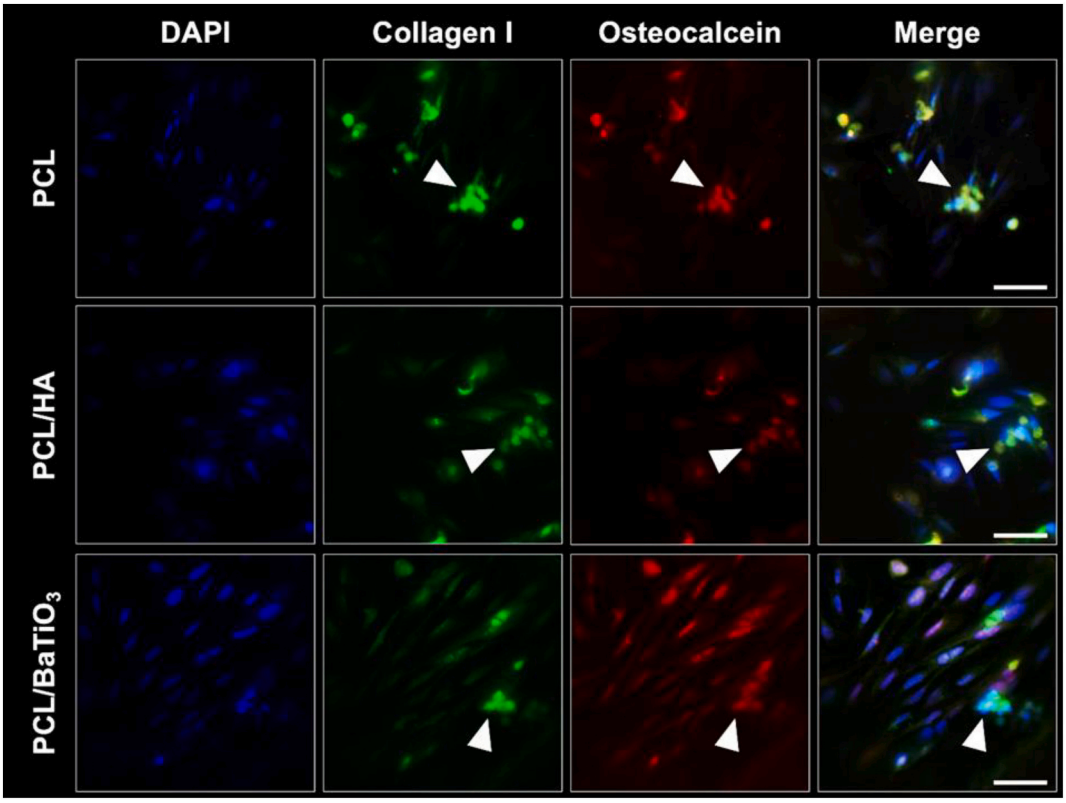

Fig. 10. Collagen and osteocalcein deposition by Saos-2 cells in PCL, PCL/HA and PCL/$BaTiO_3$ scaffolds after 28 days of culture. Fluorescent images of nucleus (blue), collagen I (green), and osteocalcein (red) and composite image to detect difference in extracellular matrix deposition in tested scaffolds. Scale bars: 50 μm. (For interpretation of the references to colour in this figure legend, the reader is referred to the web version of this article.)

PCL/HA, PCL/$BaTiO_3$), indicating that the inclusion of the bioceramic phases increases the level of mineralisation of Saos-2 cells on the scaffold [63,64].

Immunofluorescent staining images confirm the deposition of osteogenic extracellular matrix by Saos-2 cells, with the presence of Collagen-I (green) and osteocalcin (red) detected after 28 days of culture in the presence of mineralisation media (Fig. 10). Of note, scaffolds were fixed with PFA only and not permeabilised to stain only extracellular components and avoid detection of intracellular components. However, intracellular signal was still detected and observed in acquired images, and could be explained due to loss of membrane integrity during the fixation process as reported in other studies [65,66]. A punctuated extracellular staining is visible close to cells (Fig. 10), demonstrating that the surface characteristics of tested scaffolds preserve the osteoblastic phenotype with deposition of bone-like extracellular matrix onto the scaffolds. In particular, the presence of osteocalcin deposition indicates culture maturation and validates mineralisation capacity of Saos-2 cells in all scaffolds, with no clear difference across the three compositions tested. Collagen I is also deposited in all the scaffolds, with a slight increase in signal observed in PCL/$BaTiO_3$ composite scaffolds (PCL/HA $<$ PCL $\leq$ PCL/$BaTiO_3$).

4. Conclusions

Electroactive biomaterials have been demonstrated to play a significant role on natural bone pathway. In this work, for the first time PCL/$BaTiO_3$ composite scaffolds were produced by using a single-step extrusion-based 3D printing technology. Scaffolds with an interconnected structure and a high level of integrity among the inner layers were successfully manufactured, as demonstrated by the morphological analysis. Mechanical properties and porosity values were found in the range of human cancellous bone. Significantly, the inclusion of 10% wt. $BaTiO_3$ particles into the polymeric matrix improved the mechanical performance of the scaffolds, and also increased dielectric permittivity and decreased the dielectric loss. The bioactive surface of these scaffolds promoted Saos-2 osteoblast cells adhesion and proliferation, with distinctive ALP activity and deposition of osteocalcin and collagen I.

Overall, these results have highlighted the potential of multi-material additive manufacturing as promising technology towards the processing of composite electroactive biomaterials and their use in load bearing tissue engineering applications. This strategy holds great promise for sustainability by reducing material waste, the stages of the product development cycle and finally the manufacturing costs associated. Initiated by this study, future work will be performed to further investigate the use of higher concentration of $BaTiO_3$ particles into the polymeric matrix to closely mimic bone tissue properties, and the role of electrical stimulation on cellular response to obtain a functional bone tissue unit.

CRediT authorship contribution statement

Elena Mancuso: Conceptualization, Methodology, Investigation, Resources, Validation, Supervision, Writing - Review & Editing,

Lekha Shah: Investigation, Formal analysis, Data Curation, Writing - Original Draft

Swati Jindal: Investigation, Formal analysis, Data Curation, Writing - Original Draft

Cecile Serenelli: Investigation, Formal analysis

Zois Michail Tsikriteas: Investigation, Formal analysis, Data Curation, Writing - Original Draft

Hamideh Khanbareh: Methodology, Supervision, Writing - Original Draft

Annalisa Tirella: Methodology, Resources, Data Curation, Validation, Supervision, Writing - Review & Editing,

Declaration of competing interest

The authors declare that they have no known competing financial interests or personal relationships that could have appeared to influence the work reported in this paper.

Acknowledgements

The authors would like to thank Dr. John Kelly (Ulster University, UK) for the support with the mechanical characterisation, Dr. Olga Tsikou (The University of Manchester, UK) for the provision of Saos-2 cells, and both Dr. Līga Stīpniece and Dr. Kristīne Šalma-Ancāne (Riga Technical University, Latvia) for having supplied the HA powder. This work was financially supported by Ulster University (Research Challenge Fund, 2018 competition) and The North West Centre for Advanced Manufacturing (NW CAM) Project, a European Union's INTERREG VA Programme, managed by the Special EU Programmes Body (SEUPB). The views and opinions in this document do not necessarily reflect those of the European Commission or the Special EU Programmes Body (SEUPB). If you would like further information about NWCAM please contact the lead partner, Catalyst, for details.

References

[1] A.S. Brydone, D. Meek, S. Maclaine, Bone grafting, orthopaedic biomaterials, and the clinical need for bone engineering, Proc. Inst. Mech. Eng. H 224 (2010) 1329–1343, https://doi.org/10.1243/09544119JEIM770.
[2] A.R. Amini, C.T. Laurencin, S.P. Nukavarapu, Bone tissue engineering: recent advances and challenges, Crit. Rev. Biomed. Eng. 40 (2012) 363–408. https://www.ncbi.nlm.nih.gov/pmc/articles/PMC3766369/. (Accessed 3 February 2021).
[3] H.C. Pape, A. Evans, P. Kobbe, Autologous bone graft: properties and techniques, J. Orthop. Trauma 24 (Suppl. 1) (2010) S36–S40, https://doi.org/10.1097/BOT.0b013e3181cec4a1.
[4] S. Stevenson, Enhancement of fracture healing with autogenous and allogeneic bone grafts, Clin. Orthop. Relat. Res. (1998) S239–S246, https://doi.org/10.1097/00003086-199810001-00024.
[5] R. Dimitriou, E. Jones, D. McGonagle, P.V. Giannoudis, Bone regeneration: current concepts and future directions, BMC Med. 9 (2011) 66, https://doi.org/10.1186/1741-7015-9-66.
[6] J. Henkel, M.A. Woodruff, D.R. Epari, R. Steck, V. Glatt, I.C. Dickinson, P.F. M. Choong, M.A. Schuetz, D.W. Hutmacher, Bone regeneration based on tissue engineering conceptions — a 21st century perspective, Bone Res. 1 (2013) 216–248, https://doi.org/10.4248/BR201303002.
[7] G. Turnbull, J. Clarke, F. Picard, P. Riches, L. Jia, F. Han, B. Li, W. Shu, 3D bioactive composite scaffolds for bone tissue engineering, Bioact. Mater. 3 (2017) 278–314, https://doi.org/10.1016/j.bioactmat.2017.10.001.
[8] E.M. Gonçalves, F.J. Oliveira, R.F. Silva, M.A. Neto, M.H. Fernandes, M. Amaral, M. Vallet-Regí, M. Vila, Three-dimensional printed PCL-hydroxyapatite scaffolds filled with CNTs for bone cell growth stimulation, J Biomed Mater Res B Appl Biomater 104 (2016) 1210–1219, https://doi.org/10.1002/jbm.b.33432.
[9] D. Pierantozzi, A. Scalzone, S. Jindal, L. Stīpniece, K. Šalma-Ancāne, K. Dalgarno, P. Gentile, E. Mancuso, 3D printed Sr-containing composite scaffolds: effect of structural design and material formulation towards new strategies for bone tissue engineering, Compos. Sci. Technol. 191 (2020) 108069, https://doi.org/10.1016/j.compscitech.2020.108069.
[10] H. Kemppi, M.A. Finnilä, G.S. Lorite, M. Nelo, J. Juuti, M. Kokki, H. Kokki, J. Räsänen, A. Mobasheri, S. Saarakkala, Design and development of poly-L/D-lactide copolymer and barium titanate nanoparticle 3D composite scaffolds using breath figure method for tissue engineering applications, Colloids Surf. B: Biointerfaces 199 (2021) 111530, https://doi.org/10.1016/j.colsurfb.2020.111530.
[11] K. Kapat, Q.T.H. Shubhra, M. Zhou, S. Leeuwenburgh, Piezoelectric nano-biomaterials for biomedicine and tissue regeneration, Adv. Funct. Mater. 30 (2020) 1909045, https://doi.org/10.1002/adfm.201909045.
[12] B. Tandon, J.J. Blaker, S.H. Cartmell, Piezoelectric materials as stimulatory biomedical materials and scaffolds for bone repair, Acta Biomater. 73 (2018) 1–20, https://doi.org/10.1016/j.actbio.2018.04.026.
[13] M. Acosta, N. Novak, V. Rojas, S. Patel, R. Vaish, J. Koruza, G.A. Rossetti, J. Rödel, $BaTiO_3$ -based piezoelectrics: fundamentals, current status, and perspectives, Appl. Phys. Rev. 4 (2017), 041305, https://doi.org/10.1063/1.4990046.
[14] A.H. Rajabi, M. Jaffe, T.L. Arinzeh, Piezoelectric materials for tissue regeneration: a review, Acta Biomater. 24 (2015) 12–23, https://doi.org/10.1016/j.actbio.2015.07.010.
[15] Y. Li, X. Dai, Y. Bai, Y. Liu, Y. Wang, O. Liu, F. Yan, Z. Tang, X. Zhang, X. Deng, Electroactive $BaTiO_3$ nanoparticle-functionalized fibrous scaffolds enhance osteogenic differentiation of mesenchymal stem cells, Int. J. Nanomedicine 12 (2017) 4007–4018, https://doi.org/10.2147/IJN.S135605.
[16] A. Ehterami, M. Kazemi, B. Nazari, P. Saraeian, M. Azami, Fabrication and characterization of highly porous barium titanate based scaffold coated by Gel/HA nanocomposite with high piezoelectric coefficient for bone tissue engineering applications, J. Mech. Behav. Biomed. Mater. 79 (2018) 195–202, https://doi.org/10.1016/j.jmbbm.2017.12.034.
[17] J. Liu, X. Hu, H. Dai, Z. San, F. Wang, L. Ren, G. Li, Polycaprolactone/calcium sulfate whisker/barium titanate piezoelectric ternary composites for tissue reconstruction, Adv. Compos. Lett. 29 (2020), https://doi.org/10.1177/2633366X19897923, 2633366X19897923.
[18] I. Jun, H.-S. Han, J.R. Edwards, H. Jeon, Electrospun fibrous scaffolds for tissue engineering: viewpoints on architecture and fabrication, Int. J. Mol. Sci. 19 (2018), https://doi.org/10.3390/ijms19030745.
[19] M.P. Nikolova, M.S. Chavali, Recent advances in biomaterials for 3D scaffolds: a review, Bioact. Mater. 4 (2019) 271–292, https://doi.org/10.1016/j.bioactmat.2019.10.005.
[20] G.L. Koons, M. Diba, A.G. Mikos, Materials design for bone-tissue engineering, Nat. Rev. Mater. 5 (2020) 584–603, https://doi.org/10.1038/s41578-020-0204-2.
[21] P. Chocholata, V. Kulda, V. Babuska, Fabrication of scaffolds for bone-tissue regeneration, Materials (Basel) 12 (2019), https://doi.org/10.3390/ma12040568.
[22] A.-V. Do, B. Khorsand, S.M. Geary, A.K. Salem, 3D printing of scaffolds for tissue regeneration applications, Adv. Healthc. Mater. 4 (2015) 1742–1762, https://doi.org/10.1002/adhm.201500168.
[23] P. Ahangar, M.E. Cooke, M.H. Weber, D.H. Rosenzweig, Current biomedical applications of 3D printing and additive manufacturing, Appl. Sci. 9 (2019) 1713, https://doi.org/10.3390/app9081713.
[24] S.-S.D. Carter, P.F. Costa, C. Vaquette, S. Ivanovski, D.W. Hutmacher, J. Malda, Additive biomanufacturing: an advanced approach for periodontal tissue regeneration, Ann. Biomed. Eng. 45 (2017) 12–22, https://doi.org/10.1007/s10439-016-1687-2.
[25] H. Qu, Additive manufacturing for bone tissue engineering scaffolds, Mater. Today Commun. 24 (2020) 101024, https://doi.org/10.1016/j.mtcomm.2020.101024.
[26] D. Liu, W. Nie, D. Li, W. Wang, L. Zheng, J. Zhang, J. Zhang, C. Peng, X. Mo, C. He, 3D printed PCL/SrHA scaffold for enhanced bone regeneration, Chem. Eng. J. 362 (2019) 269–279, https://doi.org/10.1016/j.cej.2019.01.015.
[27] J.L. Dávila, M.S. Freitas, P. Inforçatti Neto, Z.C. Silveira, J.V.L. Silva, M.A. d'Ávila, Fabrication of PCL/β-TCP scaffolds by 3D mini-screw extrusion printing, J. Appl. Polym. Sci. 133 (2016), https://doi.org/10.1002/app.43031 n/a–n/a.
[28] A. Gelmi, C.E. Schutt, Stimuli-responsive biomaterials: scaffolds for stem cell control, Adv. Healthc. Mater. 10 (2021) 2001125, https://doi.org/10.1002/adhm.202001125.
[29] L.C. Hsiao, A.Z.M. Badruddoza, L.-C. Cheng, P.S. Doyle, 3D printing of self-assembling thermoresponsive nanoemulsions into hierarchical mesostructured hydrogels, Soft Matter 13 (2017) 921–929, https://doi.org/10.1039/C6SM02208A.
[30] R.D. Santis, A. Gloria, T. Russo, U. D'Amora, S. Zeppetelli, A. Tampieri, T. Herrmannsdörfer, L. Ambrosio, A route toward the development of 3D magnetic scaffolds with tailored mechanical and morphological properties for hard tissue regeneration: preliminary study, in: Virtual and Physical Prototyping 6, 2011, pp. 189–195, https://doi.org/10.1080/17452759.2011.631324.
[31] D.G. Tamay, T. Dursun Usal, A.S. Alagoz, D. Yucel, N. Hasirci, V. Hasirci, 3D and 4D printing of polymers for tissue engineering applications, Front. Bioeng. Biotechnol. 7 (2019), https://doi.org/10.3389/fbioe.2019.00164.
[32] C. Polley, T. Distler, R. Detsch, H. Lund, A. Springer, A.R. Boccaccini, H. Seitz, 3D printing of piezoelectric barium titanate-hydroxyapatite scaffolds with interconnected porosity for bone tissue engineering, Materials. 13 (2020) 1773, https://doi.org/10.3390/ma13071773.
[33] C. Chen, X. Wang, Y. Wang, D. Yang, F. Yao, W. Zhang, B. Wang, G.A. Sewvandi, D. Yang, D. Hu, Additive manufacturing of piezoelectric materials, Adv. Funct. Mater. 30 (2020) 2005141, https://doi.org/10.1002/adfm.202005141.
[34] S.M. Bittner, B.T. Smith, L. Diaz-Gomez, C.D. Hudgins, A.J. Melchiorri, D.W. Scott, J.P. Fisher, A.G. Mikos, Fabrication and mechanical characterization of 3D printed vertical uniform and gradient scaffolds for bone and osteochondral tissue engineering, Acta Biomater. 90 (2019) 37–48, https://doi.org/10.1016/j.actbio.2019.03.041.
[35] S.M. Bittner, J.L. Guo, A. Melchiorri, A.G. Mikos, Three-dimensional printing of multilayered tissue engineering scaffolds, Mater. Today 21 (2018) 861–874, https://doi.org/10.1016/j.mattod.2018.02.006.
[36] K.K. Gómez-Lizárraga, C. Flores-Morales, M.L. Del Prado-Audelo, M.A. Álvarez-Pérez, M.C. Piña-Barba, C. Escobedo, Polycaprolactone- and polycaprolactone/ceramic-based 3D-bioplotted porous scaffolds for bone regeneration: a comparative study, Mater. Sci. Eng. C 79 (2017) 326–335, https://doi.org/10.1016/j.msec.2017.05.003.
[37] N. Ashammakhi, S. Ahadian, C. Xu, H. Montazerian, H. Ko, R. Nasiri, N. Barros, A. Khademhosseini, Bioinks and bioprinting technologies to make heterogeneous and biomimetic tissue constructs, Mater. Today Bio. 1 (2019) 100008, https://doi.org/10.1016/j.mtbio.2019.100008.
[38] L. Moroni, J.R. de Wijn, C.A. van Blitterswijk, 3D fiber-deposited scaffolds for tissue engineering: influence of pores geometry and architecture on dynamic mechanical properties, Biomaterials. 27 (2006) 974–985, https://doi.org/10.1016/j.biomaterials.2005.07.023.
[39] M. Neufurth, X. Wang, S. Wang, R. Steffen, M. Ackermann, N.D. Haep, H. C. Schröder, W.E.G. Müller, 3D printing of hybrid biomaterials for bone tissue engineering: calcium-polyphosphate microparticles encapsulated by polycaprolactone, Acta Biomater. 64 (2017) 377–388, https://doi.org/10.1016/j.actbio.2017.09.031.

[40] M. Porta, C. Tonda-Turo, D. Pierantozzi, G. Ciardelli, E. Mancuso, Towards 3D multi-layer scaffolds for periodontal tissue engineering applications: addressing manufacturing and architectural challenges, Polymers. 12 (2020) 2233, https://doi.org/10.3390/polym12102233.
[41] X. Jin, D. Sun, M. Zhang, Y. Zhu, J. Qian, Investigation on FTIR spectra of barium calcium titanate ceramics, J. Electroceram. 22 (2009) 285–290, https://doi.org/10.1007/s10832-007-9402-1.
[42] K. Chrissafis, D. Bikiaris, Can nanoparticles really enhance thermal stability of polymers? Part I: an overview on thermal decomposition of addition polymers, Thermochim. Acta 523 (2011) 1–24, https://doi.org/10.1016/j.tca.2011.06.010.
[43] H. Qu, H. Fu, Z. Han, Y. Sun, Biomaterials for bone tissue engineering scaffolds: a review, RSC Adv. 9 (2019) 26252–26262, https://doi.org/10.1039/C9RA05214C.
[44] H. Yuk, X. Zhao, A new 3D printing strategy by harnessing deformation, instability, and fracture of viscoelastic inks, Adv. Mater. 30 (2018) 1704028, https://doi.org/10.1002/adma.201704028.
[45] A. Zimmerling, Z. Yazdanpanah, D.M.L. Cooper, J.D. Johnston, X. Chen, 3D printing PCL/nHA bone scaffolds: exploring the influence of material synthesis techniques, Biomater. Res. 25 (2021) 3, https://doi.org/10.1186/s40824-021-00204-y.
[46] A. Di Luca, A. Longoni, G. Criscenti, C. Mota, C. van Blitterswijk, L. Moroni, Toward mimicking the bone structure: design of novel hierarchical scaffolds with a tailored radial porosity gradient, Biofabrication. 8 (2016), 045007, https://doi.org/10.1088/1758-5090/8/4/045007.
[47] Q.M. Li, I. Magkiriadis, J.J. Harrigan, Compressive strain at the onset of densification of cellular solids, J. Cell. Plast. 42 (2006) 371–392, https://doi.org/10.1177/0021955X06063519.
[48] A. Ali, A. Andriyana, Properties of multifunctional composite materials based on nanomaterials: a review, RSC Adv. 10 (2020) 16390–16403, https://doi.org/10.1039/C9RA10594H.
[49] L. Zhang, G. Yang, B.N. Johnson, X. Jia, Three-dimensional (3D) printed scaffold and material selection for bone repair, Acta Biomater. 84 (2019) 16–33, https://doi.org/10.1016/j.actbio.2018.11.039.
[50] L. Tian, Z. Zhang, B. Tian, X. Zhang, N. Wang, Study on antibacterial properties and cytocompatibility of EPL coated 3D printed PCL/HA composite scaffolds, RSC Adv. 10 (2020) 4805–4816, https://doi.org/10.1039/C9RA10275B.
[51] F. Olate-Moya, L. Arens, M. Wilhelm, M.A. Mateos-Timoneda, E. Engel, H. Palza, Chondroinductive alginate-based hydrogels having graphene oxide for 3D printed scaffold fabrication, ACS Appl. Mater. Interfaces 12 (2020) 4343–4357, https://doi.org/10.1021/acsami.9b22062.
[52] A. Bagchi, S.R.K. Meka, B.N. Rao, K. Chatterjee, Perovskite ceramic nanoparticles in polymer composites for augmenting bone tissue regeneration, Nanotechnology. 25 (2014) 485101, https://doi.org/10.1088/0957-4484/25/48/485101.
[53] V.J. Hegde, O. Gallot-Lavallée, L. Heux, Dielectric study of polycaprolactone: a biodegradable polymer, in: 2016 IEEE International Conference on Dielectrics (ICD), 2016, pp. 293–296, https://doi.org/10.1109/ICD.2016.7547602.
[54] F. Kremer, A. Schönhals (Eds.), Broadband Dielectric Spectroscopy, Springer-Verlag, Berlin Heidelberg, 2003, https://doi.org/10.1007/978-3-642-56120-7.
[55] O. Vryonis, D.L. Anastassopoulos, A.A. Vradis, G.C. Psarras, Dielectric response and molecular dynamics in epoxy-BaSrTiO3 nanocomposites: effect of nanofiller loading, Polymer. 95 (2016) 82–90, https://doi.org/10.1016/j.polymer.2016.04.050.
[56] T. Tanaka, M. Kozako, N. Fuse, Y. Ohki, Proposal of a multi-core model for polymer nanocomposite dielectrics, IEEE Trans. Dielectr. Electr. Insul. 12 (2005) 669–681, https://doi.org/10.1109/TDEI.2005.1511092.
[57] E.M. Czekanska, M.J. Stoddart, R.G. Richards, J.S. Hayes, In search of an osteoblast cell model for in vitro research, Eur. Cell. Mater. 24 (2012) 1–17, https://doi.org/10.22203/eCM.v024a01.
[58] M. Prideaux, A.R. Wijenayaka, D.D. Kumarasinghe, R.T. Ormsby, A. Evdokiou, D. M. Findlay, G.J. Atkins, $SaOS_2$ osteosarcoma cells as an in vitro model for studying the transition of human osteoblasts to osteocytes, Calcif. Tissue Int. 95 (2014) 183–193, https://doi.org/10.1007/s00223-014-9879-y.
[59] W.E.G. Müller, E. Tolba, H.C. Schröder, B. Diehl-Seifert, T. Link, X. Wang, Biosilica-loaded poly(ϵ-caprolactone) nanofibers mats provide a morphogenetically active surface scaffold for the growth and mineralization of the osteoclast-related SaOS-2 cells, Biotechnol. J. 9 (2014) 1312–1321, https://doi.org/10.1002/biot.201400277.
[60] N. Ayobian-Markazi, T. Fourootan, M.J. Kharazifar, Comparison of cell viability and morphology of a human osteoblast-like cell line (SaOS-2) seeded on various bone substitute materials: an in vitro study, Dent. Res. J. (Isfahan). 9 (2012) 86–92, https://doi.org/10.4103/1735-3327.92959.
[61] G.S. Stein, J.B. Lian, A.J. Van Wijnen, J.L. Stein, M. Montecino, A. Javed, S. K. Zaidi, D.W. Young, J.Y. Choi, S.M. Pockwinse, Runx2 control of organization, assembly and activity of the regulatory machinery for skeletal gene expression, Oncogene. 23 (2004) 4315–4329, https://doi.org/10.1038/sj.onc.1207676.
[62] A. Rutkovskiy, K.-O. Stensløkken, I.J. Vaage, Osteoblast differentiation at a glance, Med. Sci. Monit. Basic Res. 22 (2016) 95–106, https://doi.org/10.12659/msmbr.901142.
[63] S.-W. Tsai, W.-X. Yu, P.-A. Hwang, Y.-W. Hsu, F.-Y. Hsu, Fabrication and characteristics of PCL membranes containing strontium-substituted hydroxyapatite nanofibers for guided bone regeneration, Polymers (Basel) 11 (2019), https://doi.org/10.3390/polym11111761.
[64] Q. Zhang, Y. Ji, W. Zheng, M. Yan, D. Wang, M. Li, J. Chen, X. Yan, Q. Zhang, X. Yuan, Q. Zhou, Electrospun nanofibers containing strontium for bone tissue engineering, J. Nanomater. 2020 (2020) e1257646, https://doi.org/10.1155/2020/1257646.
[65] R. Thavarajah, V.K. Mudimbaimannar, J. Elizabeth, U.K. Rao, K. Ranganathan, Chemical and physical basics of routine formaldehyde fixation, J. Oral. Maxillofac. Pathol. 16 (2012) 400–405, https://doi.org/10.4103/0973-029X.102496.
[66] R. Cheng, F. Zhang, M. Li, X. Wo, Y.W. Su, W. Wang, Influence of fixation and permeabilization on the mass density of single cells: a surface plasmon resonance imaging study, Front. Chem. 7 (2019) 588, https://doi.org/10.3389/fchem.2019.00588.